Editors' Suggestion

Quantum Oscillations of Nonlinear Electrical Transport in a Topological Dirac Semimetal

Vijaysankar Kalappattil,[1] Chuanpu Liu,[1] Zhijie Chen,[2] Vipul Sharma,[1] Kai Liu,[2] Jinke Tang,[3] Steven S.-L. Zhang,[4,*] and Mingzhong Wu[1,5,6,†]

[1]Department of Physics, Northeastern University, Boston, Massachusetts 02115, USA
[2]Department of Physics, Georgetown University, Washington, DC 20057, USA
[3]Department of Physics and Astronomy, University of Wyoming, Laramie, Wyoming 82071, USA
[4]Department of Physics, Case Western Reserve University, Cleveland, Ohio, 44106, USA
[5]Department of Electrical and Computer Engineering, Northeastern University, Boston, Massachusetts 02115, USA
[6]Quantum Materials and Sensing Institute, Northeastern University, Burlington, Massachusetts 01803, USA

(Received 26 September 2025; revised 31 December 2025; accepted 26 January 2026; published 4 March 2026)

Quantum oscillations in electrical transport have long served as a powerful probe of fundamental Fermi surface physics. To date, however, such studies have been restricted to linear electrical transport. This letter presents the experimental observation of quantum oscillations in nonlinear electrical transport and, more importantly, demonstrates their ability to uncover key features of the Fermi surface that lie beyond the reach of linear-transport quantum-oscillation techniques. Using α-Sn, a topological Dirac semimetal known to support both linear and nonlinear transport, this study shows that quantum oscillations of nonlinear resistance are highly sensitive to both the geometry and spin texture of the Fermi contour—features to which linear counterparts are insensitive. Further, nonlinear-transport oscillations exhibit markedly distinct dependencies on magnetic field and temperature compared to their linear analogs. These findings establish nonlinear-transport quantum oscillations as a transformative tool for exploring Fermi surface physics, opening new avenues for revealing hidden Fermi surface properties in known materials and discovering new exotic electronic states and phases.

DOI: 10.1103/bx8j-zk47

When a material is subjected to a strong magnetic field, its electronic bands are quantized into discrete Landau levels, resulting in periodic resistance variations with field strength. This phenomenon, known as quantum oscillations, has played a pivotal role in shaping modern condensed matter physics. It has enabled experimental validation of fundamental quantum mechanical principles (e.g., Landau quantization and Fermi liquid theory). It also facilitates the extraction of crucial Fermi surface properties (e.g., Fermi wave number and quantum lifetime) through electrical transport measurements, which has advanced the discovery of new materials including unconventional superconductors [1–4], topological materials [5–8], two-dimensional (2D) materials [9–13], and strongly correlated insulating states [14].

To date, studies of quantum oscillations in electrical transport have primarily focused on linear transport, where the current density (J) scales linearly with the electric field (E) following Ohm's law. However, in systems with spin-orbit coupling and broken inversion symmetry, nonlinear electrical transport naturally coexists with linear transport, giving rise to behaviors such as $J = c_1E + c_2E^2$, where c_1 and c_2 are constants [15–27]. Remarkably, quantum oscillations associated with nonlinear transport have never been reported.

This Letter presents the experimental observation of quantum oscillations in nonlinear electrical transport and, more importantly, demonstrates their ability to probe essential Fermi surface properties that are inaccessible to conventional linear-transport quantum-oscillation studies. The experiments utilize thin films of the topological Dirac semimetal α-Sn, a material known for exhibiting both linear and nonlinear transport [20]. The results reveal that nonlinear-transport quantum oscillations provide direct sensitivity to the geometry and spin orientation of the Fermi surface—features that are beyond the reach of traditional linear-transport quantum-oscillation techniques. This distinction, illustrated in Fig. 1, is further supported by theoretical calculations. In addition, nonlinear-transport quantum oscillations exhibit markedly different dependencies on magnetic field strength and temperature, diverging from their linear counterparts.

Three points should be highlighted. (1) Recent years have witnessed the observation of nonlinear electrical transport across a wide range of materials that include semiconductors [15], topological insulators [16–18], Weyl semimetals [19], topological Dirac semimetals [20], 2D electron gas systems [21], and heterostructures with

*Contact author: sxz675@case.edu
†Contact author: min.wu@northeastern.edu

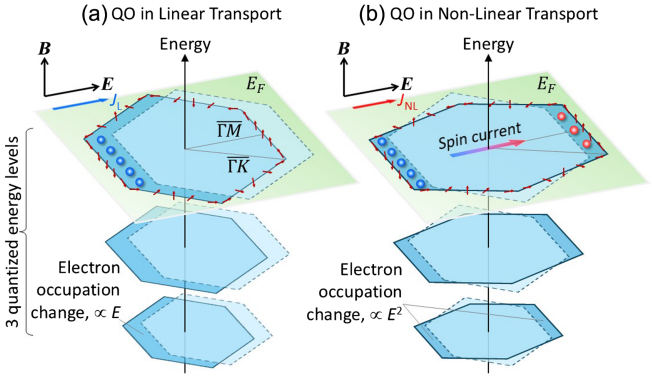

FIG. 1. Schematic comparison of quantum oscillations (QO) in linear and nonlinear transport. A magnetic field (B) quantizes the energy of electronic states. As B increases, the quantized levels cross the Fermi level (E_F), leading to resistance oscillations. (a) The first-order modification of electron distribution by an electric field (E) creates an excess of spin-down electrons (blue spheres) in left-moving states, generating a linear charge current ($J_L \propto E$). The resulting QO are sensitive only to the Fermi contour area. (b) Second-order modifications produce excess spin-down electrons in left-moving states and spin-up electrons (red spheres) in right-moving states, establishing a spin current. The magnetic field converts this spin current to a nonlinear charge current ($J_{NL} \propto E^2$). Since the spin-current polarization is governed by the spin texture (dark red arrows) at E_F, the corresponding QO are sensitive to Fermi contour geometry and spin orientation. The dashed and solid hexagons denote the Fermi contours at $E = 0$ and $E \neq 0$, respectively.

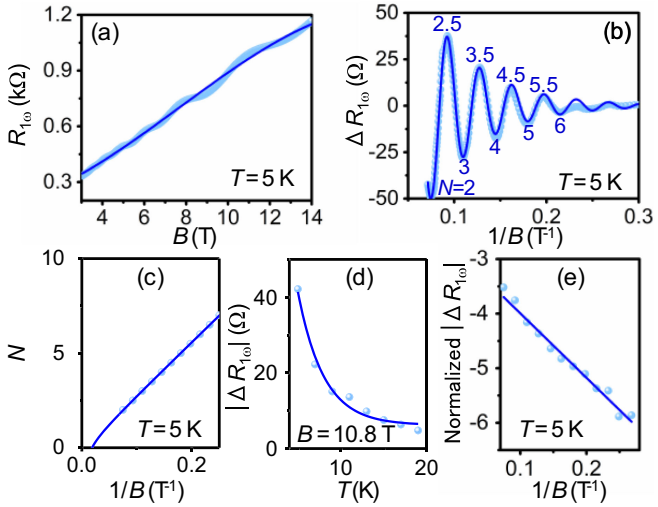

FIG. 2. Quantum oscillations of linear transport in a 5-nm α-Sn film. (a) First-harmonic resistance $R_{1\omega}$ as a function of magnetic field B. (b) Oscillation component ($\Delta R_{1\omega}$) of the data in (a) as a function of B^{-1}. (c) Landau fan diagram. (d) Amplitudes of the first oscillation peaks at different temperatures (T). (e) Dingle plot, with the vertical axis showing $\ln\{[|\Delta R_{1\omega}| \sinh(\lambda)]/(4R_0\lambda)\}$.

inversion asymmetry [22–27]. It is anticipated that this work will inspire a new wave of studies in these systems, leveraging nonlinear-transport quantum oscillations to uncover Fermi surface properties that have remained hidden until now. (2) This work also calls for the development of new theories capable of extracting key parameters (e.g., spin tilting angle, spin scattering rates, and Fermi contour curvature) from experimental nonlinear-transport quantum-oscillation data. (3) This work opens a new avenue for discovering exotic electronic states, mirroring the role that linear quantum oscillations have played in the discovery of topological materials and high-temperature superconductors [1–8].

Additionally, it is worth highlighting an earlier work experimental work reporting nonlinear-transport quantum oscillations arising in a self-heating regime [28]. Those oscillations appear in the third-harmonic response, in contrast to the nonheating regime and second-harmonic signals observed in the present study.

A common method for characterizing linear and nonlinear transport is to measure longitudinal first- and second-harmonic resistances $R_{1\omega}$ and $R_{2\omega}$, respectively, in response to an alternating current $I(t) = I_0 \cos(\omega t)$, where I_0 is the amplitude and ω is the frequency [16,19–23,27]. The $R_{1\omega}$ and $R_{2\omega}$ data ($\omega/2\pi = 21$ Hz) in this work are mostly measured on 5-nm-thick α-Sn films, grown on Si substrates and residing in a topological Dirac semimetal phase, under a perpendicular magnetic field (B). In a simplified framework, the bulk states in the α-Sn films manifest as Dirac cones with the Dirac points positioned slightly above the Fermi level, while the surface states have their Dirac points slightly below the Fermi level [29–31].

Figure 2 shows the linear-transport quantum-oscillation data, from which several key electronic properties can be extracted. Figure 2(a) gives the raw $R_{1\omega}$ data (points) and a fifth-order polynomial fit (curve) of the nonoscillating background. The residuals of this fit, denoted as $\Delta R_{1\omega}$, are presented as points in Fig. 2(b). The curve in Fig. 2(b) is a fit to [32–35]

$$\Delta R_{1\omega}\left(\frac{1}{B}\right) = |\Delta R_{1\omega}| \cos\left[2\pi\left(\frac{f}{B} - \frac{1}{2} + \frac{\varphi_0}{2\pi}\right)\right], \quad (1)$$

where f is the oscillation frequency and φ_0 is the Berry phase. The amplitude $|\Delta R_{1\omega}|$ can be expressed as

$$|\Delta R_{1\omega}| = 4AR_0 \frac{\lambda}{\sinh(\lambda)} e^{-\frac{\pi m^*}{eB\tau_q}}, \quad (2)$$

where $\lambda = (2\pi^2 k_B T m^*/\hbar e B)$, A is a scaling factor [32], k_B is the Boltzmann constant, T is temperature, m^* is the cyclotron effective mass, $\hbar$ is the reduced Planck constant, and τ_q is the quantum lifetime. Fitting in Fig. 2(b) enables the determination of the Landau index N. The N vs $(1/B)$ response is plotted in Fig. 2(c). Figures 2(d) and 2(e) reveal the decay of the oscillations with T and $(1/B)$, respectively. Figure 2(d) presents the amplitudes of the strongest peaks. The data in Fig. 2(e) are consistent with

$$\ln\left(\frac{|\Delta R_{1\omega}|\sinh(\lambda)}{4R_0\lambda}\right) = -\frac{\pi m^*}{e\tau_q}\frac{1}{B} + \ln(A). \quad (3)$$

The analysis of Fig. 2 yields φ_0, m^*, τ_q, quantum mobility μ_q, and effective Fermi wave number k_F. The fitting in Fig. 2(b) gives $f = 28.58 \pm 0.04$ T. Considering $f = (\hbar/2\pi e)A_F$ where $A_F = \pi k_F^2$ is the area enclosed by the Fermi contour, one then finds $k_F = 2.95 \times 10^8$ m^{-1}. Further, a fit of the data in Fig. 2(c) to $N = (f/B) + cB - \frac{1}{2} + (\varphi_0/2\pi)$ (c, a constant) [31,36,37] yields $f = 28.08 \pm 0.03$ T, which agrees with the above value, and $\varphi_0 = 3.28 \pm 0.01$, which is close to π. Finally, fitting of the data in Fig. 2(d) to Eq. (2) gives $m^* = 2.1 \times 10^{-31}$ kg, and fitting of the data in Fig. 2(e) to Eq. (3) gives $\tau_q = 0.46$ ps. As such, one then obtains $\mu_q = (e\tau_q/m^*) = 3380$ cm^2/(V · s).

This analysis, together with additional data in the Supplemental Material [38], indicates that the quantum oscillations originate from topological surface states (TSS) in the α-Sn film, rather than bulk states, as justified below. (1) k_F is close to the one for the TSS and is notably smaller than that for the bulk states. (2) m^* aligns more closely to the value expected for the TSS than for the bulk states. (3) The critical field (B_c) for oscillation onset is estimated to be ~4 T for the TSS and ~11 T for the bulk. The data in Fig. 2(b) show $B_c \approx 4$ T, which matches the value for the TSS. (4) The dependence of f on the field angle agrees with that expected for 2D surface states [38,45,46]. (5) The good fit in Fig. 2(b) suggests a single oscillation frequency. This means that the oscillations arise from one carrier type, indicating that the oscillations are from the TSS.

Figure 3 presents the key result of this work—the first observation of second-order transport quantum oscillations. The data were collected during the same measurements as the data in Fig. 2. Figure 3(a) shows $V_{2\omega}$, the coefficient of $\cos(2\omega t)$ in Eq. (1) in Appendix A, measured at different I_0, with the points representing the data and the curve indicating a quadratic fit. Figure 3(b) shows $R_{2\omega}$ (i.e., $V_{2\omega}/I_0$) as a function of I_0, with the points representing the data and the line indicating a linear fit. The nonlinear behavior in Fig. 3(a) and the linear dependence in Fig. 3(b) justify the use of $R_{2\omega}$ to characterize the nonlinear transport.

In Fig. 3(c), the points present a $R_{2\omega}(B)$ response measured at $I_0 = 1 \times 10^{-5}$ A and $T = 5$ K, while the curve provides a second-order polynomial fit to the background. The difference between the data and the fit, referred to as $\Delta R_{2\omega}$, is displayed in Fig. 3(d) and clearly exhibits oscillations. Figure 3(e) presents the fast Fourier transform of the data in Fig. 3(d), while Fig. 3(f) presents the indices (N) and corresponding fields of the peaks and valleys in Fig. 3(d). The presence of a single prominent peak in Fig. 3(e), combined with the linear scaling in Fig. 3(f), strongly suggests that the oscillations are due to a single type of carrier.

The oscillations in Fig. 3 represent the central finding of this work—the observation of quantum oscillations in

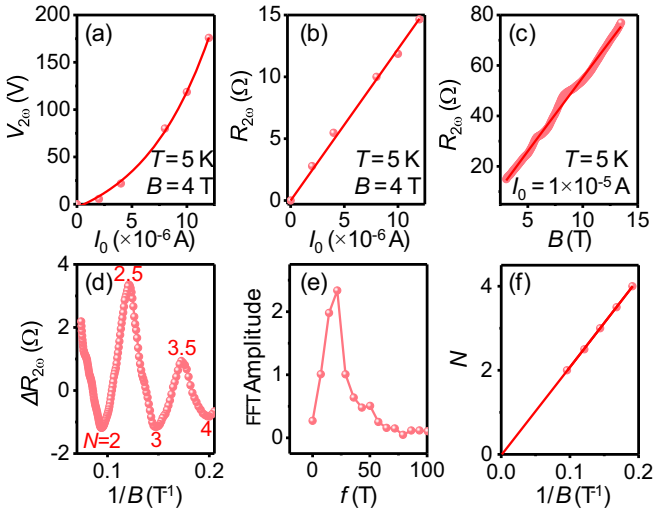

FIG. 3. Quantum oscillations of nonlinear transport in a 5-nm α-Sn film. (a) Second-harmonic voltage $V_{2\omega}$ as a function of ac amplitude I_0. (b) Second-harmonic resistance $R_{2\omega}$ as a function of I_0. (c) $R_{2\omega}$ as a function of B. (d) Oscillation component ($\Delta R_{2\omega}$) of the data in (c) as a function of B^{-1}. (e) Fast Fourier transform of the data in (d). (f) Indexes (N) and fields of the peaks and dips in (d).

nonlinear transport. Moreover, the oscillations originate from the TSS, akin to the linear-transport responses discussed earlier. This is because $R_{2\omega}$ in α-Sn is primarily associated with the TSS, as demonstrated previously [20]. As modeled in [17] and supported by experiments in [16,18–20], the application of a field E to a topological material can generate a nonlinear spin current in the TSS that scales with E^2 [see Fig. 1(b)]. This behavior contrasts with the conventional charge current produced by the same field, which scales linearly with E [see Fig. 1(a)]. In the presence of a magnetic field, the spin current can convert into a charge current, augmenting the conventional charge current and resulting in a nonlinear resistance ($R_{2\omega}$).

The data in Fig. 3 are particularly intriguing, as they mark the first observation of second-order transport quantum oscillations. Even more compelling is their remarkable sensitivity to specific Fermi surface properties that remain inaccessible to their linear-transport counterparts, as elucidated below.

In topological materials with trigonal or hexagonal crystal structures oriented along the c axis or cubic structures oriented along [111], the threefold rotational symmetry leads to hexagonal warping of the momentum-space surface Fermi contour (see Fig. 1) [47–51]. Along the hexagonal contour, the spin texture displays distinct behaviors: at the midpoint of one side (e.g., $\bar{M}$ point in Fig. 4), the spin tilts above the plane; as it progresses toward a vertex (e.g., $\bar{K}$ point in Fig. 4), the spin rotates into the plane; and at the midpoint of the next side (e.g., $\bar{M}'$ point), the spin tilts below the plane. To explore how this unique geometry of the Fermi surface and the corresponding spin texture

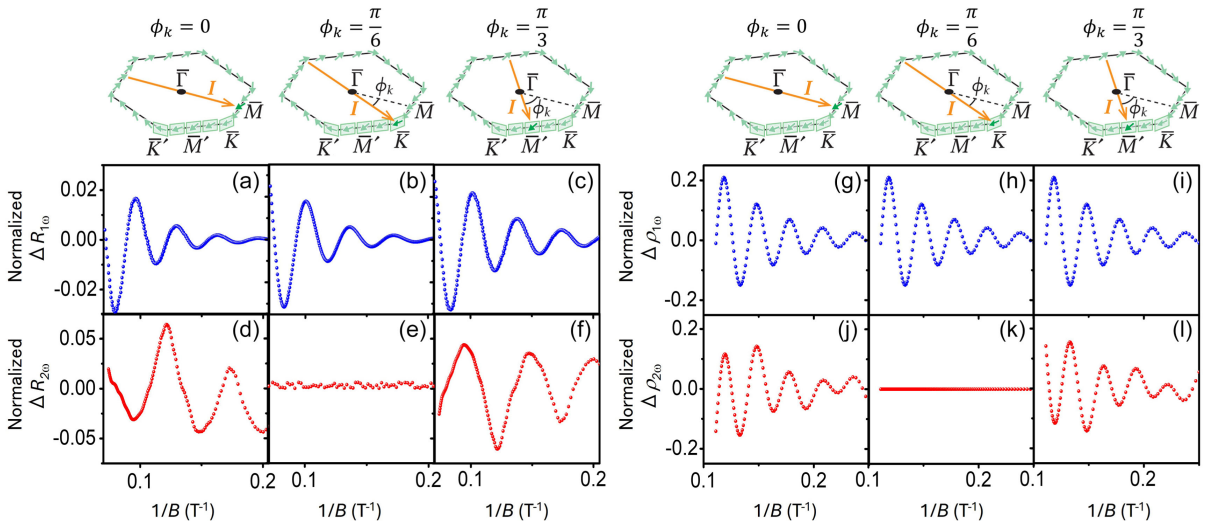

FIG. 4. Linear- and nonlinear-transport quantum oscillations for currents applied along $\bar{\Gamma}\bar{M}$, $\bar{\Gamma}\bar{K}$, and $\bar{\Gamma}\bar{M}'$ directions. (a)–(c) Measured oscillations of first-harmonic resistance. (d)–(f) Measured oscillations of second-harmonic resistance. (g)–(i) Calculated oscillations of first-harmonic resistivity. (j)–(l) Calculated oscillations of second-harmonic resistivity. All the data are normalized to their corresponding nonoscillating backgrounds.

influence the TSS' quantum oscillations, measurements were performed with currents applied along various directions in momentum space, with data shown in Figs. 4 and 6.

Figure 4 consists of two panels: the left displays experimental data, while the right presents theoretical results. In the left, the first row shows the oscillations of $R_{1\omega}$ for currents applied along three distinct directions, as indicated at the top. The second row presents the oscillations of $R_{2\omega}$ for the same current configurations. To maintain consistency with Figs. 2 and 3, the linear-transport data ($R_{1\omega}$) are shown in blue, while the nonlinear-transport data ($R_{2\omega}$) are in red. To directly compare experimental and theoretical results, the right panel in Fig. 4 is formatted identically to the left. However, one difference is that the first and second rows present the linear resistivity $\rho_{1\omega}$ and the nonlinear resistivity $\rho_{2\omega}$, respectively, instead of $R_{1\omega}$ and $R_{2\omega}$.

Three major results are evident in Fig. 4. First, as the current direction transitions from $\bar{\Gamma}\bar{M}$ to $\bar{\Gamma}\bar{K}$ and then to $\bar{\Gamma}\bar{M}'$, the quantum oscillations of the linear transport remain almost unchanged, while those of the nonlinear transport vary significantly-from strong oscillations in Fig. 4(d) to no oscillations in Fig. 4(e), and back to strong oscillations in Fig. 4(f). This indicates that linear-transport oscillations are insensitive to the hexagonal geometry of the Fermi contour, while nonlinear-transport oscillations are highly sensitive. In other words, measurements of $R_{2\omega}$ oscillations can distinguish whether the current points from $\bar{\Gamma}$ to the middle point of a hexagonal side or to a vertex of the contour. However, measurements of $R_{1\omega}$ oscillations cannot.

Second, the oscillations of $R_{2\omega}$ are out of phase for currents along $\bar{\Gamma}\bar{M}$ and $\bar{\Gamma}\bar{M}'$, as shown in Figs. 4(d) and 4(f). This is because the sign of $R_{2\omega}$ depends on the orientation of the out-of-plane spin component ($s_\perp$) of the TSS at E_F. If one denotes ϕ_k as the angle of the current relative to $\bar{\Gamma}\bar{M}$ as defined in the top diagrams, $s_\perp$ can be expressed as [16,47]

$$s_\perp = \frac{\cos(3\phi_k)}{\sqrt{[\cos(3\phi_k)]^2 + \left(\frac{\hbar v_F}{\xi k_F^2}\right)^2}}, \tag{4}$$

where v_F is the Fermi velocity and ξ characterizes the strength of the hexagonal warping. According to Eq. (4), one has $s_\perp(\phi_k = 0) = -s_\perp[\phi_k = (\pi/6)]$, which means that $s_\perp$ has opposite signs at the $\bar{M}$ and $\bar{M}'$ points. This analysis demonstrates that nonlinear-transport oscillations provide access to the spin texture along the Fermi contour—information unattainable through linear-transport oscillation studies.

Third, the theoretical results agree with the experimental observations, supporting the unique capabilities of nonlinear-transport quantum-oscillation measurements. Specifically, the oscillations in Figs. 4(g)–4(i) are nearly identical, confirming that the linear-transport oscillations are insensitive to the Fermi contour's hexagonal geometry and spin texture. In contrast, for the nonlinear-transport case in Figs. 4(j)–4(l), the presence of the oscillations depends on whether the current is directed toward a midpoint of a side or a vertex of the hexagonal contour, while the oscillation phase is determined by the sign of $s_\perp$.

Building on the strong distinction in sensitivity to the Fermi contour's geometry and spin texture, an even more exciting aspect is that nonlinear-transport quantum oscillations exhibit distinct dependencies on T and B, as presented below.

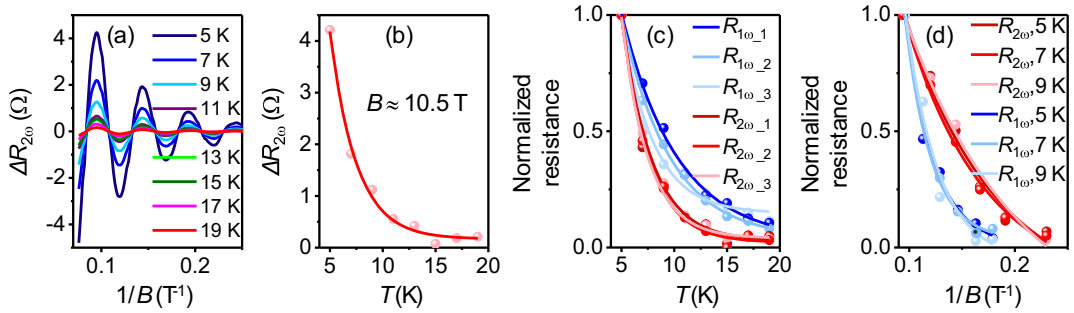

FIG. 5. Temperature (T) and field (B) dependence of quantum oscillations. (a) Oscillations of $R_{2\omega}$ measured at different T. (b) T dependence of the amplitude of the first peak in the $R_{2\omega}$ oscillation responses. (c) Comparison of the T dependences of the oscillations of $R_{1\omega}$ and $R_{2\omega}$. $R_{1\omega 1}$, $R_{1\omega 2}$, and $R_{1\omega 3}$ denote the amplitudes of the three strongest peaks in the $R_{1\omega}$ oscillations, and $R_{2\omega 1}$, $R_{2\omega 2}$, and $R_{2\omega 3}$ denote the amplitudes of the three strongest peaks in the $R_{2\omega}$ oscillations, all normalized to the values measured at 5 K. (d) Comparison of the B dependence of the oscillations of $R_{1\omega}$ and $R_{2\omega}$. The points show the peak and dip amplitudes measured at different T, all normalized to the values measured at $B \approx 10.5$ T.

Figure 5 presents the T and B dependencies of the quantum oscillations of $R_{1\omega}$ and $R_{2\omega}$. Figure 5(a) presents $R_{2\omega}$ oscillations at different T. The amplitudes of the strongest peaks in Fig. 5(a) are depicted in Fig. 5(b). To compare the T dependencies of the linear- and nonlinear-transport oscillations, Fig. 5(c) shows the amplitudes of the three strongest peaks as a function of T, with blue and red datasets for the linear and nonlinear transport, respectively. In contrast, Fig. 5(d) compares the B dependencies of the oscillations (peak amplitudes), with blue and red data sets again corresponding to the linear and nonlinear transport, respectively, as in Fig. 5(c). The curves in Figs. 5(b)–5(d) serve as visual guides. The data in Figs. 5(c) and 5(d) are normalized to the values at the lowest T and the highest B, respectively.

The data in Figs. 5(a) and 5(b) show that the oscillations of $R_{2\omega}$ decay with both T and $(1/B)$. The comparison in Fig. 5(c) demonstrates that, as T rises, the oscillations in nonlinear transport decay faster than those in linear transport. Specifically, exponential fitting to the $R_{1\omega 1}$ and $R_{2\omega 1}$ data yields a decay rate of 0.12 K^{-1} for $R_{1\omega 1}$ but a higher decay rate of 0.22 K^{-1} for $R_{2\omega 1}$. In contrast, the data in Fig. 5(d) reveal that, as B decreases, the oscillations of nonlinear transport decay slower than their linear-transport counterparts. For example, the analysis of the data measured at 5 K gives a decay rate of 36.5 T^{-1} for $R_{1\omega}$ but a lower rate of 21.3 T^{-1} for $R_{2\omega}$.

These observations further highlight the distinction between linear- and nonlinear-transport quantum oscillations, which stem from fundamentally different mechanisms. In linear transport, the decay with increasing T arises mainly from thermal broadening of the Fermi-Dirac distribution and enhanced electron scattering (e.g., with phonons). For nonlinear transport, additional processes, such as the involvement of spin currents and enhanced spin scattering at high T, contribute to the stronger decay of oscillations.

As B decreases, Landau levels get closer to each other, and disorder broadening causes them to overlap, leading to a decay of the quantum oscillations. In linear transport, oscillatory resistance is affected twice by B via the Lorentz force: first through the Hall deflection of the electrons and again when their motion is reversed and converted into additional resistance. This makes the oscillation amplitude fall off quickly, approximately as $(1/B^2)$, on top of the usual exponential Dingle damping from disorder. In nonlinear transport, the current couples more directly to the oscillatory density of states, without going through the two Lorentz-force scattering processes. This makes the decay slower, roughly as $(1/B)$.

In summary, quantum oscillations in nonlinear transport exhibit distinct characteristics compared to their linear-transport counterparts. These include high sensitivity to the Fermi contour's geometry and spin texture, more rapid decay with increasing temperature, and slower decay with decreasing magnetic field. These distinctions establish a powerful yet accessible tool for probing essential electronic properties, extending beyond the reach of conventional linear-transport quantum-oscillation experiments. Studies of quantum oscillations in nonlinear electrical transport, which can be extended to response functions beyond electric resistance (e.g., thermal conductivity), are set to propel the discovery of new exotic states of matter.

Acknowledgments—Sample fabrication, transport measurements, and data analyses were supported by the U.S. Department of Energy, Office of Science, Basic Energy Sciences, under DE-SC0018994 during the initial phase and under DE-SC0025328 during the completion phase. Theoretical work at CWRU was supported by the College of Arts and Sciences at CWRU. X-ray diffraction studies at G. U. were supported by the U.S. National Science Foundation DMR-2005108, while those at U. W. were supported by the National Science Foundation Grant No. 2228841. The authors gratefully acknowledge insightful discussions with Drs. Kin Chung Fong, Yoseob Yoon, and Xufeng Zhang.

M. W. planned the study. V. K. fabricated the devices and collected the data, with analysis performed by V. K., C. L., and M. W. Theoretical calculations were conducted by S. Z. XRD measurements were carried out by V. K., Z. C., K. L., and J. T. AFM analyses were performed by V. S. M. W., S. Z., and V. K. wrote the paper, incorporating input from all coauthors. All authors actively contributed to the discussions of the results and the preparation of the final manuscript.

Data availability—The data that support the findings of this article are openly available [52].

[1] N. Doiron-Leyraud, C. Proust, D. LeBoeuf, J. Levallois, J.-B. Bonnemaison, R. Liang, D. A. Bonn, W. N. Hardy, and L. Taillefer, Quantum oscillations and the Fermi surface in an underdoped high-T_c superconductor, Nature (London) **447**, 565 (2007).

[2] A. Alexandradinata, C. Wang, W. Duan, and L. Glazman, Revealing the topology of Fermi–surface wave functions from magnetic quantum oscillations, Phys. Rev. X **8**, 011027 (2018).

[3] Y. Cao, V. Fatemi, S. Fang, K. Watanabe, T. Taniguchi, E. Kaxiras, and P. Jarillo-Herrero, Unconventional superconductivity in magic–angle graphene superlattices, Nature (London) **556**, 43 (2018).

[4] Y. Wang, S. Hong, W. Pan, Y. Zhou, and Y. Xie, Superconducting quantum oscillations and anomalous negative magnetoresistance in a honeycomb nanopatterned oxide interface superconductor, Phys. Rev. X **15**, 011006 (2025).

[5] J. G. Checkelsky, Y. S. Hor, M.-H. Liu, D.-X. Qu, R. J. Cava, and N. P. Ong, Quantum interference in macroscopic crystals of nonmetallic Bi_2Se_3, Phys. Rev. Lett. **103**, 246601 (2009).

[6] D.-X. Qu, Y.-S. Hor, J. Xiong, R. J. Cava, and N. P. Ong, Quantum oscillations, and Hall anomaly of surface states in the topological insulator Bi_2Te_3, Science **329**, 821 (2010).

[7] B. S. Tan, Y.-T. Hsu, B. Zeng, M. Ciomaga Hatnean, N. Harrison, Z. Zhu, M. Hartstein, M. Kiourlappou, A. Srivastava, M. D. Johannes, T. P. Murphy, J.-H. Park, L. Balicas, G. G. Lonzarich, G. Balakrishnan, and S. E. Sebastian, Unconventional Fermi surface in an insulating state, Science **349**, 287 (2015).

[8] L. Zhang, X.-Y. Song, and F. Wang, Quantum oscillation in narrow-gap topological insulators, Phys. Rev. Lett. **116**, 046404 (2016).

[9] X. Cui, G.-H. Lee, Y. D. Kim, G. Arefe, P. Y. Huang, C.-H. Lee, D. A. Chenet, X. Zhang, L. Wang, F. Ye, F. Pizzocchero, B. S. Jessen, K. Watanabe, T. Taniguchi, D. A. Muller, T. Low, P. Kim, and J. Hone, Multi-terminal transport measurements of MoS_2 using a van der Waals heterostructure device platform, Nat. Nanotechnol. **10**, 534 (2015).

[10] X. Cui, E. M. Shih, L. A. Jauregui, S. H. Chae, Y. D. Kim, B. Li, D. Seo, K. Pistunova, J. Yin, J. H. Park, H. J. Choi, Y. H. Lee, K. Watanabe, T. Taniguchi, P. Kim, C. R. Dean, and J. C. Hone, Low–temperature Ohmic contact to monolayer MoS_2 by van der Waals bonded Co/h–BN electrodes, Nano Lett. **17**, 4781 (2017).

[11] D. Rhodes, S. H. Chae, R. Ribeiro-Palau, and J. Hone, Disorder in van der Waals heterostructures of 2D materials, Nat. Mater. **18**, 541 (2019).

[12] T. Smoleński, O. Cotlet, A. Popert, P. Back, Y. Shimazaki, P. Knüppel, N. Dietler, T. Taniguchi, K. Watanabe, M. Kroner, and A. Imamoglu, Interaction–induced Shubnikov–de Haas oscillations in optical conductivity of monolayer $MoSe_2$, Phys. Rev. Lett. **123**, 097403 (2019).

[13] L. Chen, A. X. Wu, N. Tulu, J. Wang, A. Juanson, K. Watanabe, T. Taniguchi, M. T. Pettes, M. A. Campbell, M. Xu, C. A. Gadre, Y. Zhou, H. Chen, P. Cao, L. A. Jauregui, R. Wu, X. Pan, and J. D. Sanchez-Yamagishi, Exceptional electronic transport and quantum oscillations in thin bismuth crystals grown inside van der Waals materials, Nat. Mater. **23**, 741 (2024).

[14] Y. Cao, V. Fatemi, A. Demir, S. Fang, S. L. Tomarken, J. Y. Luo, J. D. Sanchez-Yamagishi, K. Watanabe, T. Taniguchi, E. Kaxiras, R. C. Ashoori, and P. Jarillo-Herrero, Correlated insulator behaviour at half-filling in magic–angle graphene superlattices, Nature (London) **556**, 80 (2018).

[15] T. Guillet, C. Zucchetti, Q. Barbedienne, A. Marty, G. Isella, L. Cagnon, C. Vergnaud, H. Jaffrès, N. Reyren, J.-M. George, A. Fert, and M. Jamet, Observation of large unidirectional Rashba magnetoresistance in Ge(111), Phys. Rev. Lett. **124**, 027201 (2020).

[16] P. He, S. S. L. Zhang, D. Zhu, Y. Liu, Y. Wang, J. Yu, G. Vignale, and H. Yang, Bilinear magnetoelectric resistance as a probe of three–dimensional spin texture in topological surface states, Nat. Phys. **14**, 495 (2018).

[17] S. S.-L. Zhang and G. Vignale, Theory of bilinear magneto–electric resistance from topological–insulator surface states, Proc. SPIE Int. Soc. Opt. Eng. **10732**, 1073215 (2018).

[18] Y. Fu, J. Li, J. Papin, P. Noël, S. Teresi, M. Cosset-Chéneau, C. Grèzes, T. Guillet, C. Thomas, Y.-M. Niquet, P. Ballet, T. Meunier, J.-P. Attané, A. Fert, and L. Vila, Bilinear magnetoresistance in HgTe topological insulator: Opposite signs at opposite surfaces demonstrated by gate control, Nano Lett. **22**, 7867 (2022).

[19] P. He, C.-H. Hsu, S. Shi, K. Cai, J. Wang, Q. Wang, G. Eda, H. Lin, V. M. Pereira, and H. Yang, Nonlinear magnetotransport shaped by Fermi surface topology and convexity, Nat. Commun. **10**, 1290 (2019).

[20] Y. Zhang, V. Kalappattil, C. Liu, M. Mehraeen, S.-L. Zhang, J. Ding, U. Erugu, Z. Chen, J. Tian, K. Liu, J. Tang, and M. Wu, Large magnetoelectric resistance in the topological Dirac semimetal α-Sn, Sci. Adv. **8**, eabo0052 (2022).

[21] P. He, S. M. Walker, S. S.-L. Zhang, F. Y. Bruno, M. S. Bahramy, J. M. Lee, R. Ramaswamy, K. Cai, O. Heinonen, G. Vignale, F. Baumberger, and H. Yang, Observation of out-of-plane spin texture in a $SrTiO_3(111)$ two-dimensional electron gas, Phys. Rev. Lett. **120**, 266802 (2018).

[22] C. O. Avci, K. Garello, A. Ghosh, M. Gabureac, S. F. Alvarado, and P. Gambardella, Unidirectional spin Hall magnetoresistance in ferromagnet/normal metal bilayers, Nat. Phys. **11**, 570 (2015).

[23] C. O. Avci, K. Garello, J. Mendil, A. Ghosh, N. Blasakis, M. Gabureac, M. Trassin, M. Fiebig, and P. Gambardella,

Magnetoresistance of heavy and light metal/ferromagnet bilayers, Appl. Phys. Lett. **107**, 192405 (2015).
[24] S. S.-L. Zhang and G. Vignale, Theory of unidirectional magnetoresistance in magnetic heterostructures, Proc. SPIE Int. Soc. Opt. Eng. **10357**, 1035707 (2017).
[25] K. Yasuda, A. Tsukazaki, R. Yoshimi, K. S. Takahashi, M. Kawasaki, and Y. Tokura, Large unidirectional magnetoresistance in a magnetic topological insulator, Phys. Rev. Lett. **117**, 127202 (2016).
[26] N. H. D. Khang and P. N. Hai, Giant unidirectional spin Hall magnetoresistance in topological insulator–ferromagnetic semiconductor heterostructures, J. Appl. Phys. **126**, 233903 (2019).
[27] T.-Y. Chang, C.-L. Cheng, C.-C. Huang, C.-W. Peng, Y.-H. Huang, T.-Y. Chen, Y.-T. Liu, and C.-F. Pai, Large unidirectional magnetoresistance in metallic heterostructures in the spin transfer torque regime, Phys. Rev. B **104**, 024432 (2021).
[28] X. Huang, C. Guo, C. Putzke, J. Diaz, K. Manna, C. Shekhar, C. Felser, and P. Moll, Non-linear Shubnikov-de Haas oscillations in the self-heating regime, Appl. Phys. Lett. **119**, 224101 (2021).
[29] C.-Z. Xu, Y.-H. Chan, Y. Chen, P. Chen, X. Wang, C. Dejoie, M.-H. Wong, J. A. Hlevyack, H. Ryu, H.-Y. Kee, N. Tamura, M.-Y. Chou, Z. Hussain, S.-K. Mo, and T.-C. Chiang, Elemental topological Dirac semimetal: α-Sn on InSb(111), Phys. Rev. Lett. **118**, 146402 (2017).
[30] H. Huang and F. Liu, Tensile strained gray tin: Dirac semimetal for observing negative magnetoresistance with Shubnikov–de Haas oscillations, Phys. Rev. B **95**, 201101 (2017).
[31] Q. Barbedienne, J. Varignon, N. Reyren, A. Marty, C. Vergnaud, M. Jamet, C. Gomez-Carbonell, A. Lemaitre, P. Le Fèvre, F. Bertran, A. Taleb-Ibrahimi, H. Jaffrès, J.-M. George, and A. Fert, Angular-resolved photoemission electron spectroscopy and transport studies of the elemental topological insulator α-Sn, Phys. Rev. B **98**, 195445 (2018).
[32] G. M. Gusev, J. R. Leite, A. A. Bykov, N. T. Moshegov, V. M. Kudryashev, A. I. Toropov, and Yu. V. Nastaushev, Single-particle relaxation time in a spatially fluctuating magnetic field, Phys. Rev. B **59**, 5711 (1999).
[33] H. Murakawa, M. S. Bahramy, M. Tokunaga, Y. Kohama, C. Bell, Y. Kaneko, N. Nagaosa, H. Y. Hwang, and Y. Tokura, Detection of Berry's phase in a bulk Rashba semiconductor, Science **342**, 1490 (2013).
[34] Q. Qian, J. Nakamura, S. Fallahi, G. C. Gardner, J. D. Watson, S. Lüscher, J. A. Folk, G. A. Csáthy, and M. J. Manfra, Quantum lifetime in ultrahigh-quality GaAs quantum wells: Relationship to $\Delta_{5/2}$ and impact of density fluctuations, Phys. Rev. B **96**, 035309 (2017).
[35] R. Akiyama, K. Sumida, S. Ichinokura, R. Nakanishi, A. Kimura, K. A. Kokh, O. E. Tereshchenko, and S. Hasegawa, Shubnikov–de Haas oscillations in p and n–type topological insulator $(Bi_xSb_{1-x})_2Te_3$, J. Phys. Condens. Matter **30**, 265001 (2018).
[36] A. R. Wright and R. H. McKenzie, Quantum oscillations and Berry's phase in topological insulator surface states with broken particle-hole symmetry, Phys. Rev. B **87**, 085411 (2013).
[37] Y. Gao and Q. Niu, Zero-field magnetic response functions in Landau levels, Proc. Natl. Acad. Sci. U.S.A. **114**, 7295 (2017).
[38] See Supplemental Material at http://link.aps.org/supplemental/10.1103/bx8j-zk47 for descriptions or discussions, which includes Refs. [39–44].
[39] Ł. Gladczuk, L. Gladczuk, P. Dluzewski, G. van der Laan, and T. Hesjedal, Study of spin pumping through $\alpha-$Sn thin films, Phys. Status Solidi RRL **15**, 2100137 (2021).
[40] S. Kaku, K. L. Hiwatari, and J. Yoshino, Scanning tunneling microscopy of strained–$\alpha-\mathrm{Sn}(001)$ surface grown on InSb(001) substrate, Appl. Surf. Sci. **571**, 151347 (2022).
[41] O. Vail, P. Taylor, P. Folkes, B. Nichols, B. Haidet, K. Mukherjee, and G. de Coster, Growth and magnetotransport in thin-film α-Sn on CdTe, Phys. Status Solidi B **257**, 1800513 (2020).
[42] J. Ding, C. Liu, V. Kalappattil, Y. Zhang, O. Mosendz, U. Erugu, R. Yu, J. Tian, A. DeMann, S. B. Field, X. Yang, H. Ding, J. Tang, B. Terris, A. Fert, H. Chen, and M. Wu, Switching of a magnet by spin-orbit torque from a topological Dirac semimetal, Adv. Mater. **33**, 2005909 (2021).
[43] M. R. Scholz, V. A. Rogalev, L. Dudy, F. Reis, F. Adler, J. Aulbach, L. J. Collins-McIntyre, L. B. Duffy, H. F. Yang, Y. L. Chen, T. Hesjedal, Z. K. Liu, M. Hoesch, S. Muff, J. H. Dil, J. Schäfer, and R. Claessen, Tunable surface conductivity in the topological Dirac semimetal α-Sn, Phys. Rev. B **97**, 075101 (2018).
[44] A. Khaetskii, V. Golovach, and A. Kiefer, Revisiting the physical origin and nature of surface states in inverted-band semiconductors, Phys. Rev. B **105**, 035305 (2022).
[45] C. Zhang, A. Narayan, S.-Y. Lu, J. Zhang, Y. Zhang, X. Yuan, Z. Lin, B. Tong, G. Bian, Z. Liu, S. Jia, J. Liu, Y. Zhang, B. A. Bernevig, and Z. Wang, Transport evidence for Fermi-arc-mediated chirality transfer in the Dirac semimetal Cd_3As_2, Nature (London) **565**, 331 (2019).
[46] H. Li, P. He, Y. Cao, D. Zhang, K. He, L. Wang, H. Zhang, Q. Zhang, X. Ma, Q.-K. Xue, and Y. Wang, Quantum transport of the 2D surface state in a nonsymmorphic semimetal, Nano Lett. **19**, 815 (2019).
[47] L. Fu, Hexagonal warping effects in the surface states of the topological insulator Bi_2Te_3, Phys. Rev. Lett. **103**, 266801 (2009).
[48] K. Kuroda, M. Arita, K. Miyamoto, M. Ye, J. Jiang, A. Kimura, E. E. Krasovskii, E. V. Chulkov, H. Iwasawa, T. Okuda, K. Shimada, Y. Ueda, H. Namatame, and M. Taniguchi, Hexagonally deformed Fermi surface of the 3D topological insulator Bi_2Se_3, Phys. Rev. Lett. **105**, 076802 (2010).
[49] Z. Alpichshev, J. G. Analytis, J. H. Chu, I. R. Fisher, Y. L. Chen, Z. X. Shen, A. Fang, and A. Kapitulnik, STM imaging of electronic waves on the surface of Bi_2Te_3: Topologically protected surface states and hexagonal warping effects, Phys. Rev. Lett. **104**, 016401 (2010).
[50] Y. H. Wang, D. Hsieh, D. Pilon, L. Fu, D. R. Gardner, Y. S. Lee, and N. Gedik, Observation of a warped helical spin texture in Bi_2Se_3 from circular dichroism angle-resolved photoemission spectroscopy, Phys. Rev. Lett. **107**, 207602 (2011).
[51] M. Nomura, S. Souma, A. Takayama, T. Sato, T. Takahashi, K. Eto, K. Segawa, and Y. Ando, Relationship

between Fermi surface warping and out-of-plane spin polarization in topological insulators: A view from spin- and angle-resolved photoemission, Phys. Rev. B **89**, 045134 (2014).

[52] V. Kalappattil, C. Liu, Z. Chen, V. Sharma, K. Liu, J. Tang, S. S.-L. Zhang, and M. Wu, Quantum oscillations of nonlinear electrical transport in a topological Dirac semimetal, Dryad (2026), 10.5061/dryad.3r2280gvt.

[53] Y. Ohtsubo, S. Hatta, H. Okuyama, and T. Aruga, Tailoring the topological surface state in ultrathin α-Sn(111) films, Phys. Rev. B **100**, 245144 (2019).

End Matter

Appendix A: Characterization of linear and nonlinear electrical transport—A common method for characterizing linear and nonlinear electrical transport in a material involves measuring the longitudinal resistance in response to an alternating current (ac) [16,19–23,27]. Consider an ac in the form of $I(t) = I_0 \cos(\omega t)$, where I_0 is the current amplitude and ω is the angular frequency. If the material's resistance consists of an ordinary resistance R_0 and a nonlinear resistance $CI(t)$, where C is a constant with a unit of Ω/A, the voltage across the material can be expressed as

$$V = [I(t)][R_0 + CI(t)] = \frac{1}{2}CI_0^2 + R_0 I_0 \cos(\omega t) + \frac{1}{2}CI_0^2 \cos(2\omega t). \quad \text{(A1)}$$

Division of Eq. (1) by I_0 gives the resistance as

$$\frac{V}{I_0} = \frac{1}{2}CI_0 + R_0 \cos(\omega t) + \frac{1}{2}CI_0 \cos(2\omega t). \quad \text{(A2)}$$

In Eq. (1), the coefficients of $\cos(\omega t)$ and $\cos(2\omega t)$ describe the linear and nonlinear components, respectively, of the electrical transport. In Eq. (2), the coefficient of $\cos(\omega t)$, defined as the first-harmonic resistance $R_{1\omega}$, corresponds to the ordinary resistance, while the coefficient of $\cos(2\omega t)$, defined as the second-harmonic resistance $R_{2\omega}$, represents half of the nonlinear resistance. Thus, $R_{1\omega}$ and $R_{2\omega}$ measure the linear and nonlinear transport responses, respectively.

Appendix B: Dependence of momentum-space directions—Figure 6 presents $\Delta R_{2\omega}$ as a function of B^{-1} measured at seven current angles (ϕ_k), as indicated, at $T = 5$ K. The measurements were done with seven samples, each patterned with a Hall bar oriented along a specific direction relative to the $\bar{\Gamma}\bar{M}$ axis in the momentum space. The data clearly show that as the current direction is rotated away from the $\bar{\Gamma}\bar{M}$ direction toward the $\bar{\Gamma}\bar{M}'$ direction, $\Delta R_{2\omega}$ gradually weakens, vanishes near the $\bar{\Gamma}\bar{K}$ direction, and then reverses sign and intensifies. This angular evolution of $\Delta R_{2\omega}$ with ϕ_k evidently corroborates the results observed in Figs. 4(d)–4(f). Notably, despite the pronounced changes in oscillation amplitude, the oscillation frequency remains nearly constant across all ϕ_k values.

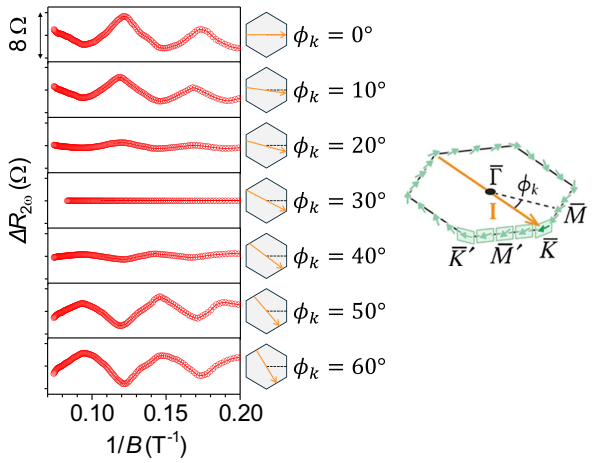

FIG. 6. Oscillations of second-harmonic resistance ($\Delta R_{2\omega}$) as a function of inverse field (B^{-1}) measured at current (I) applied along various directions relative to momentum-space orientations.

Appendix C: Thickness dependence—The data presented above were all measured with 5-nm-thick α-Sn films. Figure 7 presents the $\Delta R_{2\omega}$ vs B^{-1} profiles measured on films with four different thicknesses (d) at $T = 5$ K and $\phi_k = 0°$. The data reveal three key results. First, the 4-nm, 5-nm, and 7-nm films exhibit comparable oscillation amplitudes and nearly identical frequencies. The observation of oscillations across multiple thicknesses (Fig. 7) and for various currents in six samples (Fig. 6) confirms the robustness of the quantum

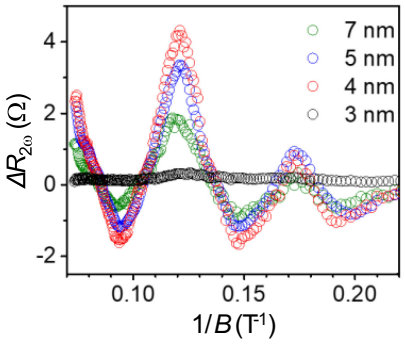

FIG. 7. Oscillations of second-harmonic resistance ($\Delta R_{2\omega}$) of as a function of inverse field (B^{-1}) measured on α-Sn films with different thicknesses, as indicated.

oscillations of $\Delta R_{2\omega}$. Second, in contrast to these three films, the one with $d = 3$ nm shows no discernible oscillations. Additional film morphology and electrical transport data suggest that this absence likely arises from strong coupling between the top and bottom TSS, and the effective thickness of the TSS in the α-Sn films studied here can therefore be estimated as about 1.5 nm [38,53]. Third, as d increases from 4 to 5 nm and then to 7 nm, the oscillation amplitude weakens. This reduction likely results from decreased film quality at larger d, as evidenced by increased surface roughness, increased resistivity, and a reduction in $R_{2\omega}$ [38].

Appendix D: Comparison of experimental and theoretical results—$\rho_{1\omega}$ and $\rho_{2\omega}$ in Fig. 4 were computed by determining the Landau levels from the warped Fermi surface first and then broadening them with a Gaussian profile to obtain a Landau-quantized density of states (DOS). The linear conductivity was calculated by integrating this DOS weighted by the derivative of the Fermi-Dirac distribution and velocity correlators, while the nonlinear conductivity includes additional terms involving higher-order energy derivatives and the inverse effective mass [38].

The experimental data in the left panel of Fig. 4 indicate that the relative oscillation amplitude of the nonlinear-transport quantum oscillations is about 2 times larger than that of the linear-transport counterparts, suggesting that the nonlinear response is more sensitive to Landau quantization. On the other hand, theory predicts comparable relative oscillation amplitudes for the linear and nonlinear resistivities, as shown in the right panel of Fig. 4. This discrepancy likely arises from the approximations inherent in the semiclassical approach, which incorporates Landau quantization only through the DOS and adopts the relaxation-time approximation. While this framework captures key features of quantum oscillations, it neglects certain quantum effects (e.g., the fine structure of the Landau level wave functions and interlevel mixing) that may also influence quantum oscillations in the nonlinear response regime.

Further, the oscillation frequencies in the theoretical results are slightly higher than those measured. This likely reflects a difference in the Fermi level, which determines the size of the Fermi surface and thus the oscillation frequency. In α-Sn, the Fermi level inferred from Hall measurements may differ from the value relevant to quantum oscillations due to contributions from multiple bands, surface-bulk hybridization, or band-bending effects. Moreover, the theoretical model used here assumes a clean, single-crystalline surface, whereas real α-Sn films contain grain boundaries and structural inhomogeneities (see Fig. S11 [38]). Such imperfections can introduce spatial variations in carrier density and local band bending, which broaden or distort the Fermi contour and shift the average Fermi level. These effects modify the effective extremal orbit area, potentially reducing the experimentally observed oscillation frequency. A more quantitative explanation of this discrepancy would require modeling these realistic sample conditions, which lies beyond the scope of the current proof-of-concept analysis. Future experimental and theoretical studies will be valuable for examining the influence of such sample-dependent effects in greater detail.